Parachutes Reefed with Sliders," *Journal of Aircraft*, Vol. 38, No. 4, 2001, pp. 818–827.

[12]Butler, M., and Crowe, M., "Design, Development and Testing of Parachutes Using the BAT Sombrero Slider," AIAA Paper 99-1708, June 1999.

[13]Potvin, J., Peek, G., Brocato, B., Perschbacher, T., and Kutz, R., "Inflation and Glide Studies of Slider-Reefed Cruciform Parachutes," AIAA Paper 2001-2021, May 2001.

[14]Richards, F. H., and Buckley, J., "Developmental Efforts of the Dual-Mode Recovery System for Integration into the Navy's System Seat Demonstrator," *Proceedings of the 32nd Annual SAFE Symposium*, 1994, pp. 164–174.

[15]Montanez, R., Potvin, J., and Peek, G., "Wind Tunnel Investigation of Ram-Air Parachute Cell Pressurization," AIAA Paper 97-1524, June 1997.

Aeroservoelastic Design Optimization with Experimental Verification

Dan Borglund*
Kungliga Tekniska Högskolan, SE-100 44 Stockholm, Sweden

Introduction

IN optimal design of structures subject to fluid-dynamic forces, the most common objective is to minimize the structural weight subject to constraints on structural stability. A recent example in aircraft structures is Eastep et al.[1] As stressed by Kuttenkeuler and Ringertz,[2] the use of optimal design methods tends to increase the likelihood of obtaining structures that are extremely sensitive to imperfections. As a consequence, possible interactions with for example a control system can have severe effects on the structural performance if not accounted for in the structural design optimization.

In aeroservoelasticity, significant efforts have been devoted to the use of active control systems to stabilize flexible aircraft structures. In particular, wing flutter suppression using aerodynamic control surfaces has been successfully demonstrated in wind-tunnel experiments, see, for example, Ghiringhelli et al.[3] However, in most such active control design the objective is to improve the performance of a structure designed without consideration of the control system.

A previous study[4] focusing on structures with internal pipe flow has indicated that significant improvements are possible in terms of reduced structural weight and control system performance by integrating the design of the control system in a structural design optimization. An integrated design optimization was performed, where the structural weight was minimized using both structural dimensions and control system parameters as design variables. In this Note the same approach is applied to the system of a cantilever flexible wing subject to unsteady aerodynamic loads.

Experimental Setup

A schematic layout of the wind-tunnel experimental setup is shown in Fig. 1. A rectangular flexible wing with semispan 1.2 m and aspect ratio 10 was mounted vertically in a low-speed wind tunnel at Kungliga Tekniska Högskolan. An electric servo was used for digital control of an aileron having approximately one-fourth the dimensions of the wing. To reduce the finite-span effects not accounted for in the numerical model (see "Aeroservoelastic Analysis"), the wing was equipped with vertical winglets as shown in Fig. 1. A detailed description of the wing geometry, structural properties, actuator performance, and the digital control system can be

*Research Associate, Department of Aeronautics. Member AIAA.
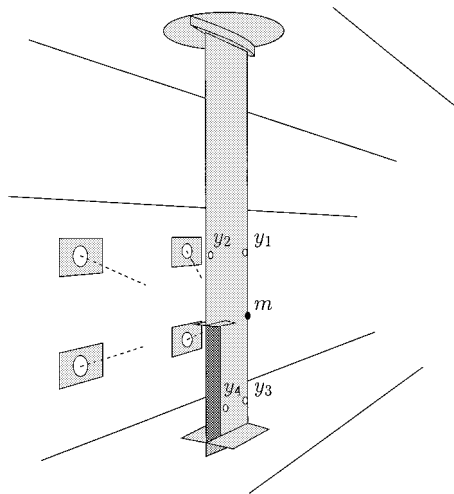
Fig. 1 Schematic layout of the wind-tunnel experiment.

found in Borglund and Kuttenkeuler.[5] The environmental conditions were room temperature and atmospheric pressure in all wind-tunnel tests. Hence, standard atmospheric conditions is used in the subsequent analysis of the wing.

The elastic deformation of the wing was monitored by a non-contact optical measurement system, capable of real-time three-dimensional tracking of reflecting markers attached to the wing. The optical system is based on four charge-coupled device cameras mounted in the wind-tunnel walls (see Fig. 1). Sufficient observability of the dominant aeroelastic modeshapes was achieved by placing two markers (y_1 and y_2) at midwing leading- and trailing-edge positions and another pair (y_3 and y_4) closer to the wing tip. Thus, the output to be used for feedback control of the wing is the four wing displacements y_1–y_4, measured by the optical system. For more details on the optical system, the reader is referred to Kuttenkeuler.[6]

Aeroservoelastic Analysis

Using beam theory for the structural dynamics, strip theory for the unsteady aerodynamic loads, and discretizing using beam finite elements,[5] the equations of motion for small elastic deformations of the wing can be written in the form

$$\dot{w} = Q(k, u)w + q\delta \qquad (1)$$

$$y = Cw \qquad (2)$$

where the dot denotes differentiation with respect to time t. The state vector $w(t)$ is composed of aeroelastic states, actuator states, and states corresponding to approximations of time delays in the digital control system. The system matrix $Q(k, u)$ is complex nonsymmetric and depends on the airspeed u and the reduced frequency $k = \omega b/u$, where w is the frequency of vibration and b the wing semichord. The setpoint for the aileron deflection is denoted $\delta(t)$, which enters the state equation through the input vector q. The measured wing displacements $y(t) = [y_1 \ y_2 \ y_3 \ y_4]^T$ are extracted from the aeroelastic states by the output matrix C.

A simple output feedback controller is defined by

$$\delta = k^T(u)y \qquad (3)$$

where $k(u)$ is a vector of four feedback gains, which are allowed to depend on the airspeed. Inserting Eqs. (3) and (2) into (1) and transforming to the frequency domain using $w(t) = \hat{w}e^{pt}$ gives the nonlinear eigenvalue problem

$$\{I\hat{p} - (b/u)[Q(k, u) + qk^T(u)C]\}\hat{w} = 0 \qquad (4)$$

where the reduced closed-loop pole (eigenvalue) $\hat{p} = pb/u$ has been introduced for convenience. The nonlinearity is caused by the dependence on the reduced frequency of oscillation $k = \omega b/u$, which is the imaginary part of $\hat{p}$. For a given airspeed u and control law $k(u)$ the eigenvalue problem (4) is solved iteratively using the so-called

p–k method.[7] The predicted critical airspeed u_{pred} at which an aeroservoelastic instability develops is computed by solving the eigenvalue problem for a sequence of increasing airspeeds until a pole with positive real part is detected.

The reduced single-input/single-output transmission zeros $\hat{z}$ from the input $\delta(t)$ to the wing displacement $y_i(t)$, $i = 1, \ldots, 4$ are computed as solutions to the generalized eigenvalue problem

$$\left[\begin{bmatrix} I & 0 \\ 0 & 0 \end{bmatrix} \hat{z} - \begin{bmatrix} (b/u)Q(k, u) & (b/u)q \\ c_i^T & 0 \end{bmatrix} \right] \begin{bmatrix} \hat{w} \\ \hat{\delta} \end{bmatrix} = \begin{bmatrix} 0 \\ 0 \end{bmatrix} \quad (5)$$

obtained by transforming Eq. (1) and $y_i(t) = c_i^T w(t) = 0$ to the frequency domain [c_i^T is the row of the output matrix C corresponding to the output $y_i(t)$]. Again, the imaginary part of $\hat{z}$ is the reduced frequency k, and this problem is solved using the p–k method as well.

Open-Loop Poles and Zeros

In Fig. 2 a root-locus plot of the leading open-loop poles and the zeros corresponding to y_1 is given. The open-loop poles are obtained by solving Eq. (4) using $k(u) = 0$, and the zeros of y_1 are obtained by solving Eq. (5) for $i = 1$. The zeros of the remaining outputs y_2, y_3, and y_4 are not presented for the sake of brevity, but follow approximately the same pattern as the zeros of y_1. The presented results were obtained using 12 finite elements in the numerical analysis. The locations of the poles and zeros at the final speed are marked by ∗ and △, respectively. A few important conclusions can be drawn from this plot. At $u = 20.7$ m/s the classical bending/torsion flutter mode becomes unstable when the pole $\hat{p}_B$ crosses the imaginary axis (marked by ○). At this speed $\hat{p}_B$ almost coalesces with the zero $\hat{z}_B$ (also marked by ○). This means that feedback of the displacement y_1 will have little influence on the mode B flutter instability.

At $u = 16.2$ m/s the two real poles $\hat{p}_D$ and $\hat{p}_E$ appear in the left-half plane. Divergence occurs at $u = 20.4$ m/s when the pole $\hat{p}_D$ crosses into the right-half plane (marked by ×). At $u = 23.3$ m/s the two real right-half plane zeros $\hat{z}_C$ and $\hat{z}_D$ appear and at $u = 23.4$ m/s $\hat{z}_D$ coalesces with the divergence pole $\hat{p}_D$ (marked by ◇). This means that even if feedback of y_1 may initially be used to stabilize the wing in divergence $u = 23.4$ m/s is an upper limit for the closed-loop critical speed as a result of reduced aileron efficiency. Increasing the speed further, $\hat{z}_D$ crosses into the left-half plane, indicating aileron reversal.

The result of the open-loop analysis is that the wing is predicted to become unstable in divergence at $u_{pred} = 20.4$ m/s, closely followed by mode B flutter at $u = 20.7$ m/s. However, in the wind-tunnel test the wing suffered a flutter instability at $u_{exp} = 16.0$ m/s. At this speed mode A in Fig. 2 is the closest to instability, and both the frequency (6.4 Hz) and the mode shape corresponds well with the experimental observation. The conclusion is that the prediction of the damping of mode A is somewhat inaccurate and that this mode becomes unstable in the experiment.
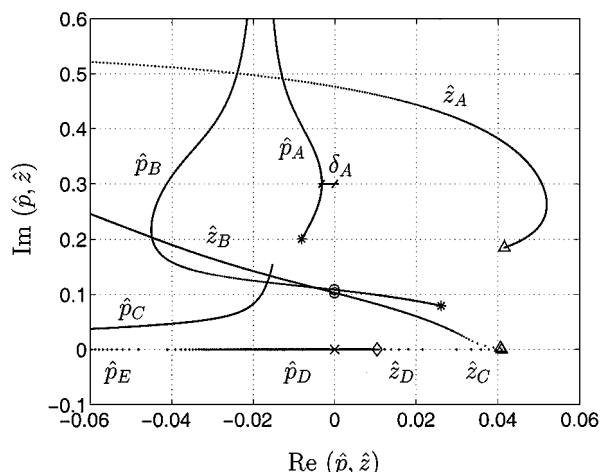
Fig. 2 Open-loop poles and zeros of y_1.

Design Optimization

The open-loop analysis indicates that the control system has only limited influence on the predicted (mode B and D) instabilities. However, it may be possible to utilize the control system to stabilize the mode A flutter instability encountered in the experiment and recover the predicted performance. The objective is thus to stabilize mode A with minimum weight penalty, using mass balancing and the control system, so that the predicted instability is observed in the experiment.

Given a set of concentrated masses m_i, $i = 1, \ldots, n_m$ at fixed locations on the wing, the problem of minimizing the weight penalty is posed as the nonlinear optimization problem

$$\text{Minimize}_{m_i, k_j} \sum_{i=1}^{n_m} m_i \quad (6)$$

$$\text{Subject to} \quad Re\,\hat{p}_A(m_i, k_j, u_j) + \delta_A \leq 0 \quad (7)$$

$$k_j^T k_j \leq k_0^2 \quad (8)$$

$$m_i \geq 0 \quad (9)$$

for $i = 1, \ldots, n_m$ and $j = 1, \ldots, n_u$. The closed-loop pole $\hat{p}_A$ is obtained by solving Eq. (4), and $\delta_A \geq 0$ is a constant stability margin that would require the pole to have strictly negative real part (see Fig. 2). No modeling of the system uncertainties is performed in this study, but a sufficient stability margin will be determined experimentally. To ensure stability up to the prescribed minimum critical speed u_{pred}, the stability constraint (7) is enforced for a discrete set of airspeeds $u_j \in [0, u_{pred}]$, $j = 1, \ldots, n_u$. The control law $k(u)$, to be determined, is discretized such that there is one set of feedback gain variables k_j for each considered airspeed u_j. For a fine discretization this results in an optimization problem with a large number of feedback gain variables. If necessary, the number of control system design variables can be reduced by using interpolating functions for the feedback gains.

A maximum feasible level of actuation is enforced by constraining the square of the 2-norm of the feedback gain vector $k(u)$ at each considered airspeed. The choice

$$k_0 = \min\{\delta_0/y_0, \dot{\delta}_0/\omega_0 y_0\} \quad (10)$$

for the maximum feasible feedback norm k_0 will result in control laws for which a servo with position and rate limits δ_0 and $\dot{\delta}_0$ will not saturate for a flutter motion with frequency $\omega \leq \omega_0$ and output norm $\|y(t)\| \leq y_0$. This result is easily derived by considering the norm of the control law (3) and the first time derivative of it.

The integrated optimization problem (6–9) is solved using the method by Svanberg,[8] and the derivatives of the stability constraint are derived as described in Haftka and Adelman.[9] The simplified problem of finding an optimal mass balancing for the open-loop system is obtained by using $k_j = 0$ in Eq. (7) and excluding the norm constraints in Eq. (8).

Solving the integrated optimization problem will provide a solution with minimum mass, which is feasible with respect to the stability constraints. However, it is not likely that maximum actuation is required to stabilize the wing at all operating conditions, in particular at low airspeeds. Only the feedback gain vectors k_j for which the constraint (8) is active are unique by means of being a stabilizing control law at the particular airspeed. At airspeeds where the norm constraint is not active, there is redundant actuation, which can be used for other purposes than reducing structural weight.

This study focus on controllers using a minimum level of actuation. The integrated design with minimum mass and a control law $k^*(u)$ with minimum norm subject to the stability constraint (7) is obtained in two steps. First, the integrated optimization problem (6–9) is solved for the optimal mass balancing m_i^*. Then the optimal control law is computed by solving a series of optimization problems minimizing the feedback norm:

$$\text{Minimize}_{k} \quad k^T k \quad (11)$$

$$\text{Subject to} \quad Re\,\hat{p}_A(m_i^*, k, u) + \delta_A \leq 0 \quad (12)$$

Solving Eqs. (11) and (12) for the airspeeds u_j considered in the integrated optimization provides a set of optimal feedback gain vectors $\boldsymbol{k}_j^*(u_j)$, which can be used for gain scheduling in the experiment. The constraint for the feedback norm is not required in this optimization problem because the structural design is such that maximum actuation will only be required for those airspeeds where the norm constraint (8) was active in the integrated optimization. Also note that a different set of airspeeds from that used in the integrated optimization can be used in this second step.

Wind-Tunnel Experiments

The maximum feasible norm of the feedback gain $k_0 = 10\pi/3$ was chosen. Using this value, the servo will persist a mode A flutter motion with output norm $y_0 = 0.02$ m without saturating.[5] Weights used for mass balancing were allowed at leading- and trailing-edge positions at the spanwise locations of the nodes in the finite element model, numerically modeled as point masses.

The first problem considered was to increase the critical speed using only mass balancing. By enforcing the stability constraint for a small set of airspeeds around 16 m/s, approximately 10 iterations were required to achieve values of the mass variables accurate to four digits. The increment $\Delta\delta_A = 0.003$ was chosen for the successive stability margins enforced in the design optimization, which corresponds to the inherent stability margin of the bare wing shown in Fig. 2. Only the leading-edge mass at the upper end of the aileron cutout, denoted m in Fig. 1, was assigned a nonzero optimal value for the problems considered. As shown in Table 1 (design 1, 2, and 3), the stability margin $\delta_A = 0.009$ was required to achieve an experimentally feasible design, which became unstable in divergence at $u_{\exp} = 23.6$ m/s (design 3).

The integrated optimization required approximately 15 iterations for the same number of stability constraints, whereas each optimization problem in the final control law design required approximately five iterations. To obtain a well-defined control law in the experiments for airspeeds higher than $u_{\text{pred}} = 20.4$ m/s, the control law optimization was simply extended without consideration of other instabilities. It should be emphasized that a controller designed exclusively for stabilizing mode A will influence the other modes as well, which is not considered in the optimization. The resulting controllers were found to have a slightly destabilizing effect on the divergence mode D, but no action was taken because this was not observed in the experiment.

With the integrated approach (design 4, 5, and 6 in Table 1) $\delta_A = 0.006$ resulted in pure flutter suppression (design 4). For the sake of brevity, the optimal control law is presented only in terms of feedback gain norm vs airspeed (see Fig. 3). However, in the experiment mode A was not stabilized as predicted, and this design turned out infeasible. The integrated approach required a stability margin $\delta_A = 0.012$ to result in a feasible design (design 6 in Table 1 and Fig. 3). This indicates that additional uncertainties are intro-

Table 1 Results from design optimization compared with experimental results

Design	δ_A, —	m, g	u_{pred}, m/s	$u_{\exp}$, m/s
1	0	0	20.4 (D)	16.0 (A)
2	0.006	19.6	20.4 (D)	18.6 (A)
3	0.009	47.0	20.4 (D)	23.6 (D)
4	0.006	0	20.4 (D)	16.6 (A)
5	0.009	11.5	20.4 (D)	18.8 (A)
6	0.012	27.3	20.4 (D)	23.6 (D)

duced when including the control system in the design optimization. Turning the control system off, a weak mode A limit-cycle motion appeared at 19 m/s, which means that mode A is in fact the most unstable at a higher speed than the predicted 16 m/s. Despite the larger stability margin, the integrated approach resulted in 42% less weight penalty compared to the optimal mass balancing.

Conclusions

The present study has demonstrated a simple case of integrated design optimization of an aeroservoelastic system. It was shown that the simultaneous structural and control system design in general requires a two-step procedure to result in a minimum weight design and a control law that is well-defined for all operating conditions.

The integrated approach required a larger stability margin to result in an experimentally feasible design because of additional uncertainties introduced when including the control system in the structural optimization. Strip theory is well known[10] to overpredict the unsteady aerodynamic loads, which is most likely the dominant uncertainty in the present system. Consequently, both the divergence speed and the speed at which mode A is the most unstable were underpredicted by approximately 15–20%. However, the essential dynamics was predicted surprisingly well by the fairly simple aeroservoelastic model, and the integrated approach resulted in a final design with 42% less weight penalty.

In a previous study[5] it was shown that by suppressing mode A with full actuation for all airspeeds, pure flutter suppression was possible. This means that imposing a constant stability margin on the reduced poles is in general not optimal and that there in this case exists an optimal stability margin $\delta_A^*(u)$ such that zero weight penalty is achievable for some minimum level of actuation. Computing such an optimal flutter margin based on a model of the system uncertainties is a challenge in itself. The concept of computing robust flutter margins begin to manifest itself as a state-of-the-art research area in aeroelasticity[11] and is of vital importance for the development of more advanced optimization methods taking uncertainties into account.

References

[1]Eastep, F. E., Tischler, V. A., Venkayya, V. B., and Khot, N. S., "Aeroelastic Tailoring of Composite Structures," *Journal of Aircraft*, Vol. 36, No. 6, 1999, pp. 1041–1047.

[2]Kuttenkeuler, J., and Ringertz, U. T., "Aeroelastic Design Optimization with Experimental Verification," *Journal of Aircraft*, Vol. 35, No. 3, 1998, pp. 505–507.

[3]Ghiringhelli, G. L., Lanz, M., and Mantegazza, P., "Active Flutter Suppression for a Wing Model," *Journal of Aircraft*, Vol. 27, No. 4, 1990, pp. 334–341.

[4]Borglund, D., "Active Nozzle Control and Integrated Design Optimization of a Beam Subject to Fluid-Dynamic Forces," *Journal of Fluids and Structures*, Vol. 13, No. 2, 1999, pp. 269–287.

[5]Borglund, D., and Kuttenkeuler, J., "Active Wing Flutter Suppression Using a Trailing Edge Flap," *Journal of Fluids and Structures* (to be published).
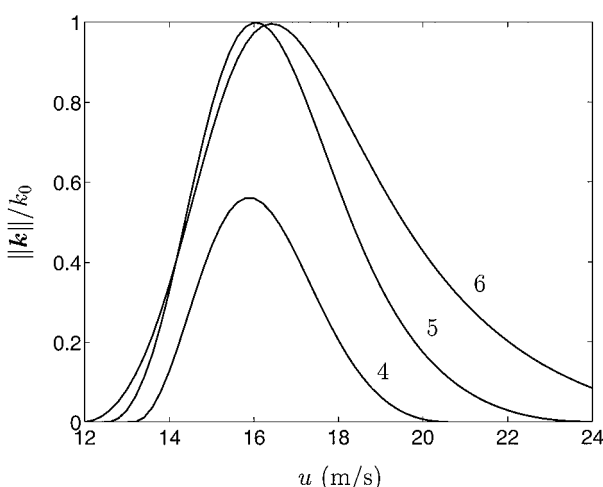
Fig. 3 Feedback gain norm vs airspeed for design 4, 5, and 6.

[6]Kuttenkeuler, J., "Optical Measurements of Flutter Mode Shapes," *Journal of Aircraft*, Vol. 37, No. 5, 2000, pp. 846–849.

[7]Bäck, P., and Ringertz, U. T., "On the Convergence of Methods for Nonlinear Eigenvalue Problems," *AIAA Journal*, Vol. 35, No. 6, 1997, pp. 1084–1087.

[8]Svanberg, K., "The Method of Moving Asymptotes (MMA) with Some Extensions," *Optimization of Large Structural Systems*, Vol. 1, Kluwer, Dordrecht, The Netherlands, 1993, pp. 555–566.

[9]Haftka, R. T., and Adelman, H. M., "Sensitivity of Discrete Systems," *Optimization of Large Structural Systems*, Vol. 1, Kluwer, Dordrecht, The Netherlands, 1993, pp. 289–311.

[10]Bisplinghoff, R. L., Ashley, H., and Halfman, R. L., *Aeroelasticity*, Dover, New York, 1996, p. 591.

[11]Lind, R., and Brenner, M., *Robust Aeroservoelastic Stability Analysis*, Springer-Verlag, London, 1999, p. 2.

Poststall Behavior of a Wing Under Externally Imposed Sound

N. A. Ahmed* and R. D. Archer†
University of New South Wales,
Sydney, New South Wales 2052, Australia

Nomenclature

$\mathcal{R}$ = aspect ratio of wing
C_D = total drag coefficient of wing
C_L = lift coefficient of wing
C_l = section lift coefficient of wing
f = acoustic frequency
Re = Reynolds number of flow based on wing chord, wind-tunnel airstream velocity, density, and dynamic viscosity
Sr = Strouhal number based on wing chord, wind-tunnel freestream velocity, and acoustic excitation frequency
α = angle of attack or incidence
δ = Glauert coefficient

I. Introduction

LIFT force can generally be augmented by an increase in wing area, angle of incidence, camber, or artificial circulation for fixed air properties and freestream. There is however, a limit as to how far these features can be exploited without encountering what is known as wing stall. Wing stall not only decreases aerodynamic efficiency of a wing, but can pose severe hazard during flight. Poststall flow behavior on a wing, therefore, is an important area of research in aerodynamics and forms the basis of this study.

Improvement of stall behavior of a wing generally involves manipulation of boundary-layer flow on its surface. In the subsonic and transonic speeds, pressure gradients can be particularly strong, and a wing can only continue to generate lift successfully beyond stall incidence, if boundary-layer separation is either delayed or avoided. Various techniques such as suction or blowing or circulation control[1−3] have been used with varying degrees of success for a long time. The concept of controlling boundary-layer separation by acoustic excitation has occurred much later and remains least developed. It was probably the finding of Spangler and Wells[4] that sound has a significant effect on boundary-layer transition that has led to various attempts[5−8] to control or suppress laminar flow separation and induce turbulent flow without going through the unstable phase of transition flow. Most of these works have involved both internal as well as external excitation, but are mainly limited to investigation

*Senior Lecturer, Aerospace Engineering.
†Professor, Aerospace Engineering. Senior Member AIAA.

of two-dimensional flows such as those encountered on flat plates or airfoils. In the present study, an attempt has been made to look at the poststall behavior of a low aspect ratio wing subjected to externally excited sound energy.

II. Experiment

A 30-in.- (0.76-m-) diam open return, low-speed open test section of 0.2% turbulence intensity wind-tunnel of the Aerodynamics Laboratory of the University of New South Wales was used in the experiments. A schematic of the experimental setup and instrumentation is given in Fig. 1. The wind tunnel was powered by a 15-bhp compound wound dc variable speed electric motor driving a fan to give a freestream velocity range of 0–30 m/s. A manometer connected to a pitot static tube was used to record the wind speed.

The acoustic signals were generated using a sine wave generator and a speaker of 15-Ω impedence, which was powered by a 21-Ω rated load amplifier of 120-W capacity. The amplifier had no gain control, and power had to be varied by varying the input voltage.

A constant section symmetric NACA 0012 half-wing of effective aspect ratio of 4 was held on one end to a two-axis force balance platform while the other end was left free. The balance was equipped with two load cells of 100-N force transducers of ±0.1-N force resolution, one measuring side or lift force and the other in the direction of the flow or the drag force. Flow visualization was carried out using smoke illuminated by a laser light sheet that used a 10-mW He–Ne laser as a light source.

Experiments were performed at 16-, 17-, 18-, and 19-deg angle of incidence using externally excited sound frequencies that ranged between 100 Hz and 3 kHz and at three Reynolds number flows of 0.7×10^5, 1×10^5, and 2.6×10^5, respectively. Flow visualization, however, was restricted to the lowest Reynolds number of 0.7×10^5 to obtain clearer photographs.

III. Results and Discussion

A. Qualitative Results: Flow Visualization

Laser light sheet visualizations of flow over the wing were carried out at the 16-, 17-, and 18-deg angle of incidence for the unexcited and excited conditions, respectively, at the Reynolds number of 0.7×10^5. Figures 2 and 3 show two visualization obtained at 16- and 18-deg angle of incidences, respectively. In Figs. 2 and 3, flow separation on the wing from the leading edge under unexcited (Figs. 2a and 3a) and its subsequent suppression under externally imposed sound (Figs. 2b and 3b) are clearly visible. With increasing angle of attack, although the streamlines over the upper surface were observed to remain parallel to the contour of the top surface in the first-half or forebody of the wing, they appear to gradually diverge away in the second-half of the wing suggesting the onset of flow separation in this region.

B. Quantitative Results

1. C_L and C_D vs Acoustic Frequency

Figure 4 shows the variation of C_L and C_D with changes in acoustic frequency at the four incidences of 16-, 17-, 18-, and 19-deg at $Re = 0.7 \times 10^5$, 1×10^5, and 2.6×10^5, respectively. The solid lines without symbols represent the C_L and C_D values under the no excitation condition.

a. Results at $Re = 0.7 \times 10^5$. At this Reynolds number Re, externally excited imposed sound produces significant improvements on the C_L and C_D values at all of the four angles of incidence (Fig. 4a). However, there are some differences that can be noted. At the lower angles of incidence, that is, at $\alpha = 16$, 17, and 18 deg, the improvements can be observed over a wide frequency range, $200 < f < 2000$ Hz, or an equivalent Strouhal number range of $5 < Sr < 45$, with a 20–30% increase in C_L values and a 20–30% decrease in C_D values resulting in a near doubling of the aerodynamic efficiency over the unexcited values. At $\alpha = 19$ deg, the effect of sound is observed in a smaller frequency range of $200 < f < 1200$ Hz, and the improvements are less pronounced with up to 15% increase in lift and 10% decrease in drag being observed.

b. Results at $Re = 1 \times 10^5$. At $Re = 1 \times 10^5$ (Fig. 4b), there is a shift of the curves compared to those observed at $Re = 0.7 \times 10^5$,